

The Launching of Cold Clouds by Galaxy Outflows. IV. Cosmic-Ray-driven Acceleration

Marcus Brüggen and Evan Scannapieco Huniversität Hamburg, Hamburger Sternwarte, Gojenbergweg 112, D-21029 Hamburg, Germany School of Earth and Space Exploration, Arizona State University, P.O. Box 871404, Tempe, AZ 85287-1404, USA Received 2020 August 7; revised 2020 October 6; accepted 2020 October 9; published 2020 December 8

Abstract

We carry out a suite of simulations of the evolution of cosmic-ray (CR) driven, radiatively cooled cold clouds embedded in hot material, as found in galactic outflows. In such interactions, CRs stream toward the cloud at the Alfvén speed, which decreases dramatically at the cloud boundary, leading to a bottleneck in which pressure builds up in front of the cloud. At the same time, CRs stream along the sides of the cloud, forming a boundary layer where large filaments develop. Shear in this boundary layer is the primary mode of cloud destruction, which is relatively slow in all cases, but slowest in the cases with the lowest Alfvén speeds. Thus, the CR pressure in the bottleneck region has sufficient time to accelerate the cold clouds efficiently. Furthermore, radiative cooling has relatively little impact on these interactions. Our simulations are two-dimensional and limited by a simplified treatment of CR dynamics, the neglect of CR heating, and an idealized magnetic field geometry. Nevertheless, our results suggest that CRs, when acting as the primary source of momentum input, are capable of accelerating clouds to velocities comparable to those observed in galaxy outflows.

Unified Astronomy Thesaurus concepts: Magnetohydrodynamical simulations (1966)

1. Introduction

Galactic winds play a key role in the cosmic cycle of matter, driving material from deep within the densest regions of galaxies into the rarified fringes of the circumgalactic medium (e.g., Davé et al. 2011; Tumlinson et al. 2017). Such winds have been studied in great detail across a wide range of galaxy masses and redshifts (e.g., Martin 1999; Pettini et al. 2001; Heckman 2002; Veilleux et al. 2005, 2020), including the ultraluminous infrared galaxies (ULIRGs) that provide as much as half of the $z \ge 1$ star formation in the universe (Rupke et al. 2005). Observations of galactic winds have revealed a complex multiphase gas ranging from $\approx 10^7$ to 10^8 K plasma observed in X-rays (e.g., Martin 1999; Strickland & Heckman 2009), to $\approx 10^4$ K material observed at optical and near-ultraviolet wavelengths (e.g., Pettini et al. 2001; Tremonti et al. 2007; Martin et al. 2012; Soto & Martin 2012), to 10–10³ K molecular gas observed at radio wavelengths (e.g., Walter et al. 2002; Bolatto et al. 2013).

The coexistence of these different phases is not easy to explain, particularly in the presence of cold material moving at supersonic velocities. Incomplete thermalization of supernova ejecta naturally causes outflows to be born as multiphase gas, but the ram-pressure acceleration of cold clouds in hot media is extremely inefficient. Instead, instabilities and evaporation lead to rapid cloud disruption well before the cold gas is significantly accelerated. In the definitive study of the nonradiating, hydrodynamic case, Klein et al. (1994) showed that if hot material moves past a cloud at a velocity $v_{\rm hot}$ that is less than the external sound speed, but greater than the cloud's internal sound speed, it will shred the cloud within $\approx 2-3$ "cloud crushing" times, defined as $t_{\rm cc} \equiv \frac{\chi_0^{1/2} R_{\rm cloud}}{v_{\rm hot}}$, where $R_{\rm cloud}$ is the cloud radius and $v_{\rm hot}/\chi_0^{1/2}$ is the velocity that the resulting shock moves through the cloud, with χ_0 the initial density ratio between the cloud and the surrounding medium.

When radiative cooling is significant, and thermal conduction is minimal, the primary mechanism for cloud disruption is the Kelvin–Helmholtz (KH) instability. This is suppressed in

supersonic flows, leading to a disruption time that scales as $t_{cc}\sqrt{1+M}$, where M is the Mach number in the ambient medium (Scannapieco & Brüggen 2015, hereafter Paper I). However, when thermal conduction is taken into account, an evaporative interface forms, stabilizing the cloud against hydrodynamical instabilities. In this case, the clouds can maintain coherent structures for a longer timescale, which can be explained by considering the balance between the internal energy that impinges on a spherical cloud and the energy of the evaporating material (Brüggen & Scannapieco 2016, hereafter Paper II). In Paper II, we also showed that thermal conduction also changes the shock jump conditions ahead of the cloud and pressure from the evaporation off the surface transforms the cloud into a cylindrical shape that leads to a larger surface, which in turn leads to more evaporation (see also Huang et al. 2020).

While magnetic fields have the potential to suppress the growth of instabilities, in practice, they do little to increase cloud lifetimes (Cottle et al. 2020, hereafter Paper III). Magnetic fields aligned with the wind slow the growth of KH modes, but the magnetic pressure also resists compression and the cloud develops a wispy tail, which mixes with the wind on a timescale similar to that in the hydrodynamic case. On the other hand, magnetic fields transverse to the wind get "draped" around the cloud, compress the cloud along the field direction, and expand it in the perpendicular direction. The result is continuous mass loss, leading to a shorter lifetime than in the hydrodynamic case. To avoid these problems, various authors have studied alternative models for the cold wind phase, such as the condensation of cold clouds out of the hot phase (e.g., Wang 1995; Silich et al. 2003; Thompson et al. 2016; Scannapieco 2017; Schneider et al. 2018), the recondensation of gas in the tails of cold clouds (e.g., Gronke & Oh 2018, 2020), and the acceleration of clouds due radiation pressure (e.g., Thompson et al. 2005; Hopkins et al. 2011; Murray et al. 2011).

Another possibility is the acceleration of cold clouds by cosmic rays (CRs). Such relativistic particles are thought to

play a role in launching galactic winds in Milky Way-type galaxies, where, unlike starbursts, the thermal gas alone is not sufficient to launch a wind. While hot, thermally driven winds are possible, their mass-loading factors are lower than for the slow CR-driven winds that advect the warm (10⁴ K) ionized gas (Girichidis et al. 2018). Similarly, radio halos in galaxies have long shown the presence of CRs and magnetic fields (e.g., Irwin et al. 1999; Wiegert et al. 2015; Heesen et al. 2019).

Several theoretical studies have indicated that CR pressure gradients can lead to outflows (Breitschwerdt et al. 1993; Everett et al. 2008; Dorfi & Breitschwerdt 2012). Hanasz et al. (2013) demonstrated that CRs alone can launch fast, magnetized winds in high surface density disks. Booth et al. (2013) and Salem & Bryan (2014) simulated the diffusion of CRs out of star-forming regions and find that this can lead to the establishment of stable vertical pressure gradients that are in line with observations. In global magnetohydrodynamic (MHD) simulations of a Milky Way–sized galaxy, Ruszkowski et al. (2017) showed that moderately super-Alfvénic CRs propagate out of denser regions along magnetic fields and thereby accelerate more tenuous gas out of the galaxy. Thus, they concluded that CRs can play an important role in reducing galactic star formation rates and launching galactic winds.

Samui et al. (2018) devised a spherically symmetric thin shell model for CR-driven outflows and showed that CRs are particularly important for driving outflows in low-mass galaxies. Using idealized simulations of the early phases of outflows, Jana et al. (2020) showed that in the early stages of galactic outflows CRs do not have any noticeable effect on the mass loading by the outflow and that in the early stages of galactic outflows the dynamical role of CRs is not important.

When Alfvén wave damping processes can be neglected, the CR streaming speed is equal to the Alfvén velocity, and CRs are locked to the wave frame. The model of CR streaming was further refined in Holguin et al. (2019) in which the authors devised a more realistic model of turbulent suppression of the streaming speed. They found that turbulent damping leads to larger scale heights of gas and CRs, and as a result the star formation rate increases with the level of turbulence in the interstellar medium (ISM). Farber et al. (2018) showed results from three-dimensional magnetohydrodynamical simulations that include the decoupling of CRs in the cold, neutral interstellar medium. They found that this decoupling leads to higher wind speed and affects wind properties such as density and temperature.

A requirement for a successful acceleration of clouds in galactic halos is that the CR pressure gradient should exceed the gravitational potential. Lacki et al. (2010) argued that the CR pressure cannot overcome gravity at high gas surface densities provided that CRs interact with the mean density of the ISM, and if pion losses dominate advection/diffusion. Wang & Fields (2018) have shown that starbursts act as proton calorimeters in which a substantial fraction of the energy in CRs injected via supernovae is lost through hadronic processes. Another location where CRs may be essential for the dynamics of cold clouds are high-velocity clouds in the CR halo of the Galaxy (Bregman 2004).

While the aforementioned papers study winds on galactic scales, there is little work on the dynamics of individual clouds in a CR-driven outflow. Recently, Wiener et al. (2019) used 2D simulations to show that a Milky Way–sized galaxy with a star formation rate of 20–30 M_{\odot} yr⁻¹ would generate enough CRs

to accelerate clouds to 100 km s⁻¹. They also find that cloud acceleration depends almost linearly on the injected CR flux.

In this paper, we study the evolution of cold clouds driven by CR pressure gradients in a magnetized medium. In a suite of two-dimensional simulations performed with the FLASH AMR MHD code (Fryxell et al. 2000), we expose cold clouds to CR gradients that are driven from one side of the computational domain. The CRs stream with Alfvén speeds along the magnetic field lines and thus interact with the cold cloud. Here, we neglect the effect of CR diffusion (both isotropic and anisotropic) as well as CR heating. To focus on the impact of the CRs themselves, we also neglect thermal conduction as well as gravity, which is negligible for the cloud densities and sizes studied here.

The structure of this work is as follows. In Section 2, we discuss the physics of CR pressure buildup and cloud acceleration and describe our numerical methods and setup. In Section 3 we present our results on the mass loss and velocity resolution and asses the impact of radiative cooling. We present our conclusions in Section 4.

2. Simulations of CR-driven Clouds

2.1. Methods

Since the scattering mean free path of individual CRs is smaller than any other relevant scale, we can treat them as a fluid. The transport equation for CRs is then given by

$$\frac{\partial p_{\text{CR}}}{\partial t} = (\gamma_{\text{CR}} - 1)(\boldsymbol{u} + \boldsymbol{v}_{\text{s}}) \cdot \nabla p_{\text{CR}}
- \gamma_{\text{CR}} \nabla \cdot [p_{\text{CR}}(\boldsymbol{u} + \boldsymbol{v}_{\text{s}})],$$
(1)

where $p_{\rm CR}$ is the CR pressure, $\gamma_{\rm CR} = 4/3$ is the ratio of the specific heats of the CRs, u is the velocity of the gas, and $v_{\rm s}$ is the streaming velocity (e.g., McKenzie & Webb 1984).

Throughout this paper, we work with the CR energy per volume, ϵ_{CR} (mass scalar times density), rather than the pressure, and we track its evolution using the equations of fluid motion. For the simulations, we employ the FLASH code, version 4.3 (Fryxell et al. 2000), and solve the following equations:

$$\frac{\partial \rho}{\partial t} + \nabla \cdot (\rho \mathbf{u}) = 0, \tag{2}$$

$$\rho \left[\frac{\partial \boldsymbol{u}}{\partial t} + (\boldsymbol{u} \cdot \nabla) \boldsymbol{u} \right] = \frac{1}{4\pi} (\boldsymbol{B} \cdot \nabla) \boldsymbol{B} - \nabla p', \tag{3}$$

$$\frac{\partial E}{\partial t} + \nabla \cdot (E\boldsymbol{u}) = -\nabla \cdot (p'\boldsymbol{u}) + \frac{1}{4\pi} \nabla \cdot [(\boldsymbol{B} \cdot \boldsymbol{u})\boldsymbol{B}], \quad (4)$$

$$\partial_t \mathbf{B} + (\mathbf{u} \cdot \nabla) \mathbf{B} = (\mathbf{B} \cdot \nabla) \mathbf{u} - \mathbf{B} (\nabla \cdot \mathbf{u}), \tag{5}$$

$$\nabla \cdot \mathbf{B} = 0, \tag{6}$$

$$\frac{\partial \epsilon_{\text{CR}}}{\partial t} + \nabla \cdot (\epsilon_{\text{CR}} \boldsymbol{u}) = -\boldsymbol{v}_{\text{s}} \cdot \nabla \epsilon_{\text{CR}}
- \gamma_{\text{CR}} \epsilon_{\text{CR}} \nabla \cdot [\boldsymbol{u} + \boldsymbol{v}_{\text{s}}] + \epsilon_{\text{CR}} \nabla \cdot \boldsymbol{u},$$
(7)

where ρ , \mathbf{u} , $p' = p + p_{\rm CR} + \frac{1}{8\pi} |\mathbf{B}|^2$, \mathbf{B} , and $E = \rho \epsilon_{\rm int} + \rho \frac{1}{2} |\mathbf{u}|^2 + \frac{1}{8\pi} |\mathbf{B}|^2$ denote density, velocity, pressure (thermal, CR, and magnetic), magnetic field, and total energy density (internal, kinetic, and magnetic). The first term on the right-hand side of Equation (4) accounts for the magnetic tension due to Lorentz forces, and the second term accounts for

the other component of the Lorentz force, the magnetic pressure. The advection of the CRs is handled by the hydro routine, and the source terms on the right-hand side are handled by a heating routine. Finally, the CRs affect the gas via $F = -\nabla p_{\rm CR} = -(\gamma_{\rm CR} - 1)\nabla\epsilon_{\rm CR}$, which for practical reasons we implement in a modified gravity routine. Equation (8) does not include a heating term caused by the streaming instability (Skilling 1975) well below our simulation resolution limits that thermalize their energy instantly in the thermal gas (sometimes also called streaming losses; Wiener et al. 2019).

We implemented optically thin cooling, using the tables compiled by Wiersma et al. (2009) from the code CLOUDY (Ferland et al. 1998), assuming solar metallicity. As in Gray & Scannapieco (2010), subcycling was implemented within the cooling routine itself, such that T and $\Lambda(T, Z)$ were recalculated every time 10% of the thermal energy was radiated away. For the mean mass per particle we took 0.6 m_p . Cooling is disabled for temperatures below $T = 10^4$ K.

Following, Sharma et al. (2009) we set the streaming velocity to

$$v_{\rm s} = -\frac{B}{\sqrt{4\pi\rho}} \tanh(l_R \nabla p_{\rm CR}/p_{\rm CR}) \frac{(\boldsymbol{B} \cdot \nabla p_{\rm CR})\hat{\boldsymbol{b}}}{|\boldsymbol{B} \cdot \nabla p_{\rm CR}|}, \tag{8}$$

where l_R is a regularization parameter that we set to $l_R = 50 \,\mathrm{kpc}$ and $\hat{\boldsymbol{b}}$ is the unit vector in the direction of the magnetic field. Unlike in Wiener et al. (2019), we also regularize the divergence of p_{CR} by the same tanh function. In addition, we require that ∇p_{CR} exceeds a threshold of 10^{-35} erg cm⁻⁴ for the *x*-component of the Alfvén velocity to turn negative. The latter condition suppresses numerical issues where tiny errors related to the computation of spatial derivatives strongly affect the results and can be physically motivated as wave damping. The time step limitation imposed by the CR streaming is given by Wiener et al. (2017):

$$dt_{\text{stream}} \sim dx^2 / l_R p_{\text{CR}} |v_{\text{A}}| = 10^{11} \left(\frac{dx}{100 \text{ pc}} \right)^2 \times \left(\frac{|v_{\text{s}}|}{200 \text{ km s}^{-1}} \right)^2 \left(\frac{l_R}{10 \text{ kpc}} \right)^{-1} \text{s.}$$
(9)

Moreover, in order to guard against small numerical fluctuations that may reverse the streaming direction of CRs, we set the CR pressure to zero wherever the CR pressure is less than 1% of the value maintained at the lower *x*-boundary.

Finally, we add a switch that allows acceleration by CRs only on cells whose density lies at least 10% above the ambient density, which suppresses the acceleration of the ambient medium by streaming against sound waves and weak shocks that develop from reflections and numerical noise. It is not immediately clear whether or not this assumption increases in accuracy of the simulation, as Alfvén velocity fluctuations due to density differences in the hot medium in real galaxies could potentially contribute to the bulk acceleration of the medium. We note, however, that (i) this is unlikely to be main mode of acceleration of the hot medium, which has a sound speed much higher than the escape velocity of the host galaxy, and hence expands freely into the surrounding environment (Chevalier & Clegg 1985; Scannapieco 2013); (ii) the density differences in the hot medium are not well modeled by the numerical noise,

and so any acceleration due to this effect in the simulations will not match those nature; and (iii) the impact of this threshold on our simulations is small, as discussed in more detail below.

2.2. Run Parameters

To better quantify the acceleration of dense clouds by CRs, we set up a simple system in 2D with a source term that maintains a constant CR pressure (equal to the thermal pressure) on the x=0 boundary. The physical size of the domain was 8 kpc in the x-direction and 3.2 kpc in the y-direction. The root grid size was 10×4 blocks of 8×8 cells and a maximum of five levels of refinements yielding an effective resolution of $\Delta x=1.6$ pc with 5120×2048 cells.

At a distance of 325 pc from the boundary, we placed a circular cloud with a radius of R=100 pc, which is equal to 64 resolution elements. The density inside the cloud was $\rho_{\rm cl}=10^{-26}$ g cm⁻³, and the ambient density was $\rho_{\rm amb}=\rho_{\rm cl}/\chi$. In order to avoid numerical artifacts at boundaries with infinite gradients in the Alfvén speed, we used Gaussian tapers at the edges of the cloud with scale lengths that equal one-fourth of the cloud radius, e.g., $\rho(r)=\rho_{\rm amb}+(\rho_{\rm cl}-\rho_{\rm amb})\exp(-r^2/l_{\rm s}^2)$, where r is the radial distance from the edge of the cloud and $l_{\rm s}$ is the scale length. The temperature inside the cloud for all runs was fixed at 10^4 K, and the temperature in the ambient gas was set by demanding that the initial thermal pressure is constant throughout the simulation volume. The Jeans mass of the cloud after shock passage at a temperature of 10^4 K and number densities of the order of $10\,{\rm cm}^{-3}$ are several $10^7 M_{\odot}$, which is more than the cloud masses considered here.

As in our previous papers in the series, we tracked the cloud using a massless scalar and computed its center-of-mass (COM) position x_c and velocity v_c , as well as its radial extent in the x- and y-directions, calculated as the mass-weighted average values of $abs(x-x_c)$ and $abs(y-y_c)$.

Outside the cloud, the magnetic field was assumed to be uniform in the *x*-direction, such that the CRs stream toward the cloud, and the field strength was set by the plasma parameter $\beta=p_{\rm therm}/p_B$. We did not investigate other magnetic field configurations. In our setup, transverse magnetic fields would not allow the CRs to reach the cloud. In a set of runs we varied the dimensionless parameters χ and β as listed in Table 1. The parameters are chosen such that the Alfvén velocity, $v_{\rm A}\sim 15~{\rm km~s^{-1}}\sqrt{\chi/\beta}\gtrsim 25,~{\rm km~s^{-1}},~{\rm i.e.},~\chi/\beta>3$. The cloud crushing time with respect to the sound speed is $\chi_0^{1/2}R_{\rm cl}/c_{\rm s},$ which is also given in Table 1. Hereafter, we use this definition of the cloud crushing time.

3. Results

3.1. Morphological Evolution

In Figure 1, we show the density of our $\chi=300$ runs at fixed cloud crushing times of 1, 5, and 10 $t_{\rm cc}$, illustrating the overall evolution of the interaction. The CRs stream toward the cloud at the Alfvén speed, which decreases dramatically at the cloud boundary. This leads to a bottleneck in which the CRs pile up in front of the cloud (e.g., Wiener et al. 2017), building up pressure, which compresses the cloud in the direction of the flow and begins accelerating it downstream.

At the same time, the CRs start to stream along the sides of the cloud, leading to a second pressure gradient. This causes the cloud to be compressed in the perpendicular direction, dragging the field lines with it and increasing the magnetic field

Table 1
Parameters of the Simulations

Name	χ	β	<i>B</i> (μG)	(km s^{-1})	$v_{\rm A}/c_{\rm s}$	t _{cc} (Myr)	$q_0 = (\text{erg cm}^{-2} \text{ s}^{-1})$	$\frac{N_c}{(\mathrm{cm}^{-2})}$
CHI300BETA100	300	100	5.9×10^{-2}	28.7	0.11	6.5	4.0×10^{-8}	6.1×10^{18}
CHI300BETA10	300	10	1.8×10^{-1}	90.9	0.35	6.5	1.3×10^{-7}	6.1×10^{18}
CHI300BETA3	300	3	3.4×10^{-1}	165.9	0.63	6.5	2.3×10^{-7}	6.1×10^{18}
CHI300BETA1	300	1	5.9×10^{-1}	287.5	1.1	6.5	4.0×10^{-7}	6.1×10^{18}
CHI100BETA10	100	10	1.8×10^{-1}	52.5	0.35	6.5	7.2×10^{-8}	6.1×10^{18}
CHI100BETA3	100	3	3.4×10^{-1}	95.8	0.63	6.5	1.3×10^{-7}	6.1×10^{18}
CHI100BETA1	100	1	5.9×10^{-1}	165.9	1.1	6.5	2.3×10^{-7}	6.1×10^{18}
CHI30BETA10	30	10	1.8×10^{-1}	28.7	0.35	6.5	4.0×10^{-8}	6.1×10^{18}
CHI30BETA3	30	3	3.4×10^{-1}	52.5	0.63	6.5	7.2×10^{-7}	6.1×10^{18}
CHI30BETA1	30	1	5.9×10^{-1}	90.9	1.1	6.5	1.3×10^{-7}	6.1×10^{18}

Note. χ is the density ratio between cloud and the ambient medium, β is the ratio of thermal to magnetic pressure, B is the magnetic field strength, v_A the Alfvén velocity in the ambient medium, v_A/c_s the ratio of the Alfvén velocity to the sound speed in the ambient medium, $t_{cc} = \chi_0^{1/2} R_{cl}/c_s$ is the cloud crushing time with respect to the sound speed, and $q_0 = p_{CR}(x=0) \cdot v_A$ is the source strength.

strength. Note that due to magnetic tension, the field lines that thread the cloud are pushed together not just within the cloud, but also in the regions of the hot medium immediately surrounding it. This leads to a region of high magnetic field strength, but low mass density in the boundary layer directly surrounding the cloud, causing the Alfvén speed to go up dramatically within these areas, as illustrated in Figure 2.

As a result, the CRs stream past the cloud, and the pressure gradient associated with the additional pressure significantly increases the downstream velocity of the gas in this layer. The flow is then divided into three regions, as can be seen in Figure 3: (i) the bottleneck region immediately in front of the cloud, in which CR pressure causes cloud acceleration but gas velocities are relatively modest; (ii) a boundary layer on the sides of the cloud, in which the CR pressure compresses the cloud perpendicular to the flow, and gas velocities are large, leading to significant shear; and (iii) the region far away from the cloud, in which CRs stream freely along the magnetic fields and the gas velocities are small.

Region (i) is most important in the acceleration of the cloud, but region (ii) is the most important in determining its morphology, as well as the cloud lifetime. This shear layer causes mass to be ablated from the cloud in long, narrow filaments that are advected downstream with the wind for several kiloparsecs, and the rate of this ablation is determined by the KH instability in the boundary region. Note that for a given density contrast, the filaments are longer for cases with lower values of β , in which the magnetic field plays a larger role in shaping the dynamics of the flow. Lower values of β also imply higher Alfvén speeds, and hence faster CR streaming. This is in contrast to the gas velocities, which depend primarily on the CR pressures and are very similar across the different $\chi=300$ runs.

Figures 4 and 5 show the evolution of the cloud density and Alfvén speed in the $\chi=30$ case, again at three representative times of 1, 5, and 10 $t_{\rm cc}$. Here the same overall evolution occurs as is seen in the $\chi=300$ runs, with a bottleneck forming in front of the cloud, followed by the development of a boundary layer with a high Alfvén speed immediately surrounding the cloud. Also as in the $\chi=300$ case, the bottleneck region is primarily responsible for cloud acceleration, while the boundary layer is responsible for most of the shear that disrupts the cloud. As the density of the medium surrounding the cloud is 10 times higher than in the previous case, and

hence the Alfvén speed is smaller, the filaments in this case are less extended than their $\chi=300$ counterparts.

Finally, Figure 6 contrasts the density evolution of runs as a function of β and χ . In general, the differences between the runs are primarily seen in the length of the filaments. These are most extended in those runs with the highest Alfvén speeds, which is $\propto \beta^{-1/2} \chi^{1/2}$ since the cloud density is the same in all cases. On the other hand, as the CR pressure is similar in all the runs, the densest regions near the front of the cloud evolve similarly, regardless of β and χ .

It is important to point out that our results differ in a several significant respects from those in Wiener et al. (2019). As they do not adopt the techniques described in Section 2.1, particularly the regularization criterion, small waves develop in the ambient medium, which impede the streaming of the CRs past the cloud, This leads to an acceleration of the gas that surrounds the dense cloud and causes a bulk flow that contributes to the acceleration of the cloud and its subsequent evolution. However, in simulations, this acceleration is dependent on numerics, and in nature, it is likely subdominant to acceleration of the hot material as it expands as free wind. As this bulk flow does not exist in our case, and instead the cloud evolution is driven by the CR pressure that builds up in front of the cloud and the shear layer that forms around the cloud, which leads to the onset of KH instabilities and the loss of mass. It is not obvious which computational setup is more realistic. In reality, CRs may well lead to the bulk acceleration of gas, but this may also not be the case, so our focus is to fully understand the evolution caused purely by the CRs themselves.

3.2. Mass Evolution

In Figure 7, we show the fraction of the mass retained by the cloud in each of the runs as a function of time in units of the cloud crushing time, $t_{\rm cc}$. More specifically, we plot $F_{1/3}(t)$, which is the fraction of the total mass at or above one-third the original cloud density as defined in Paper I. Note that in this figure and the ones below, we define t=0 at two Alfvén times from the start of the simulation, as this is the time that the CRs first encounter the front of the cloud.

As the cloud crushing time only depends on χ , the quantity $t/t_{\rm cc}$ is the same for all plots in the same panel. Hence, we find that the mass evolution at a given χ value is largely independent of β , and thus also largely independent of the

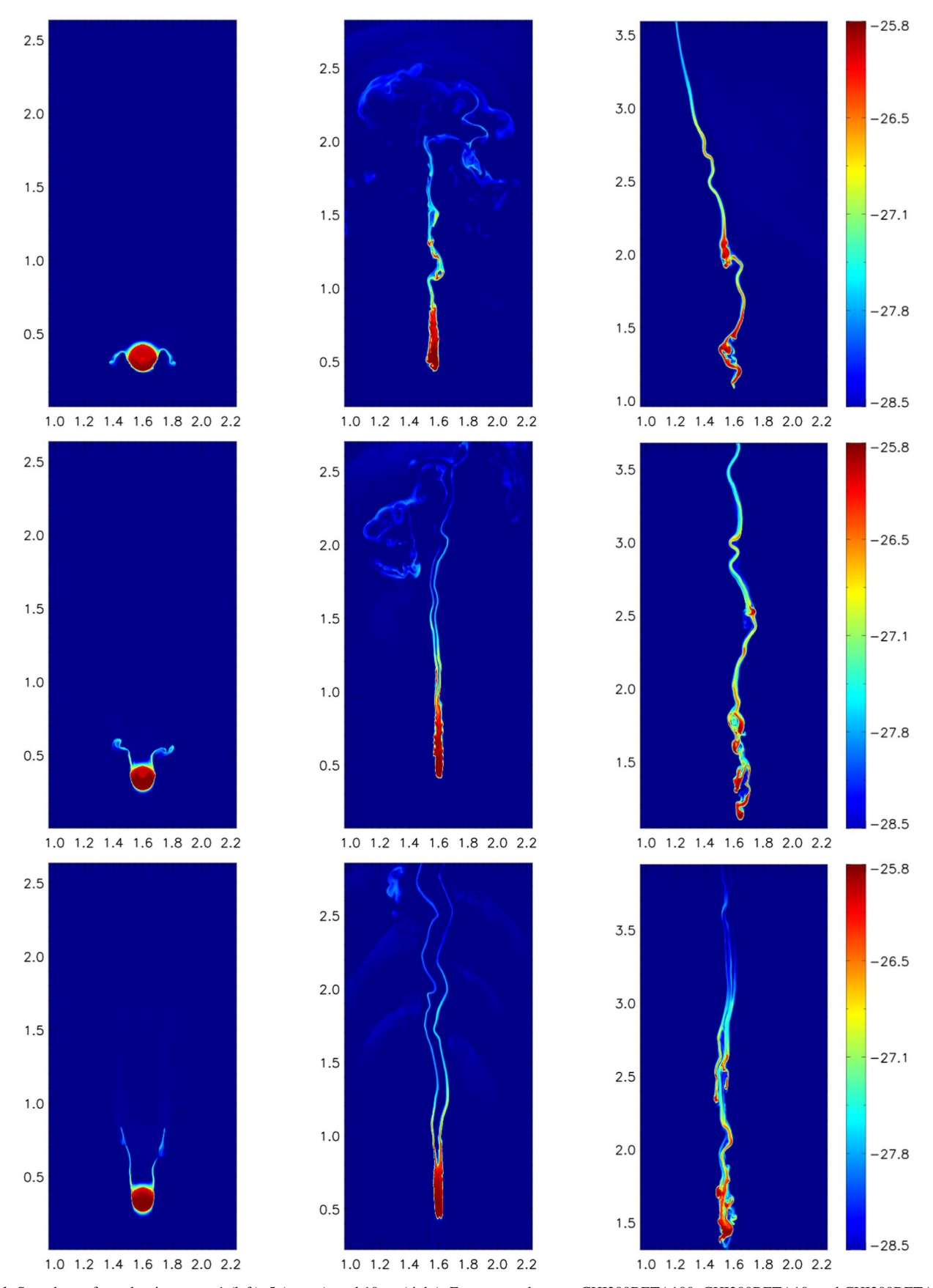
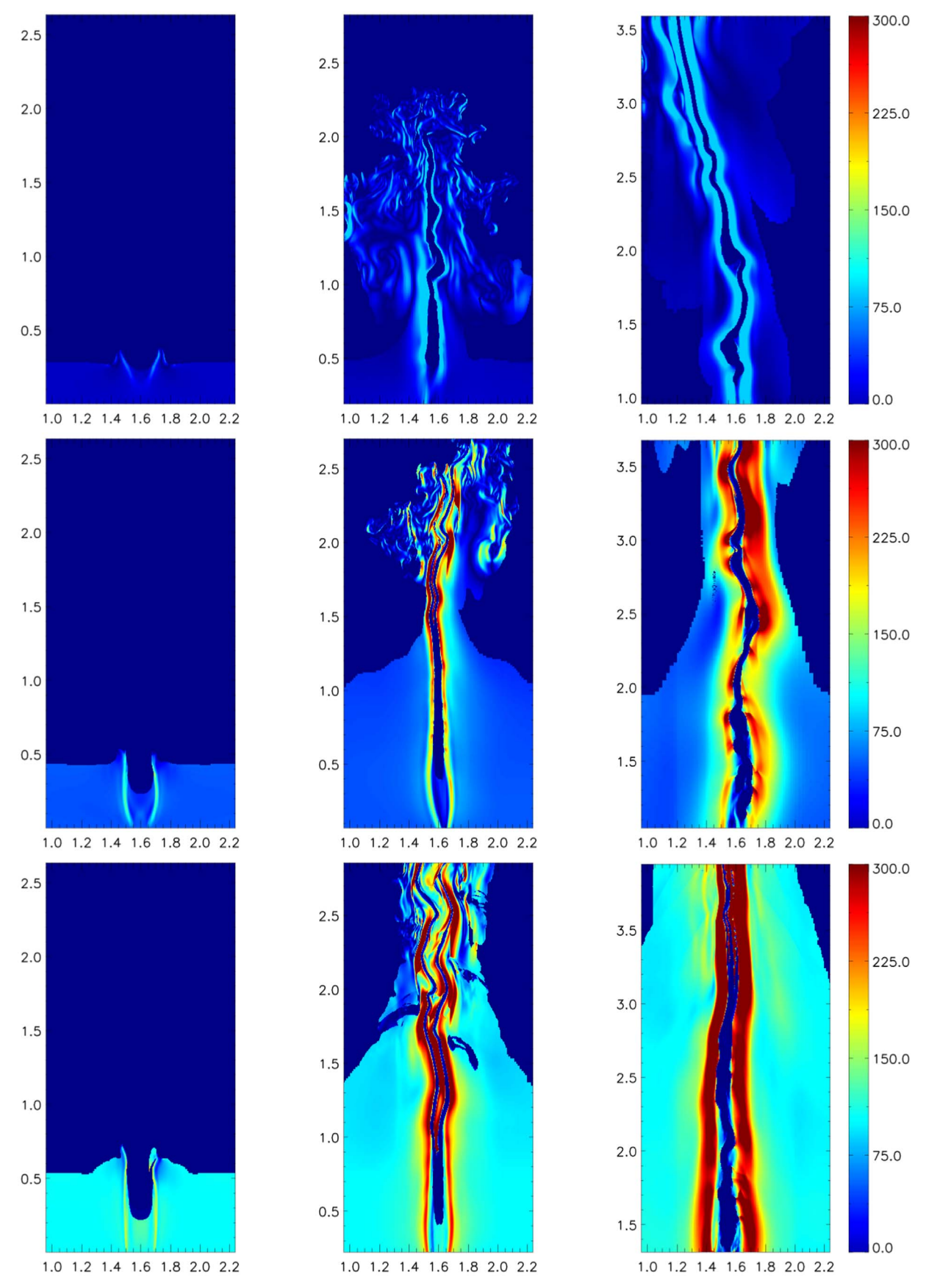
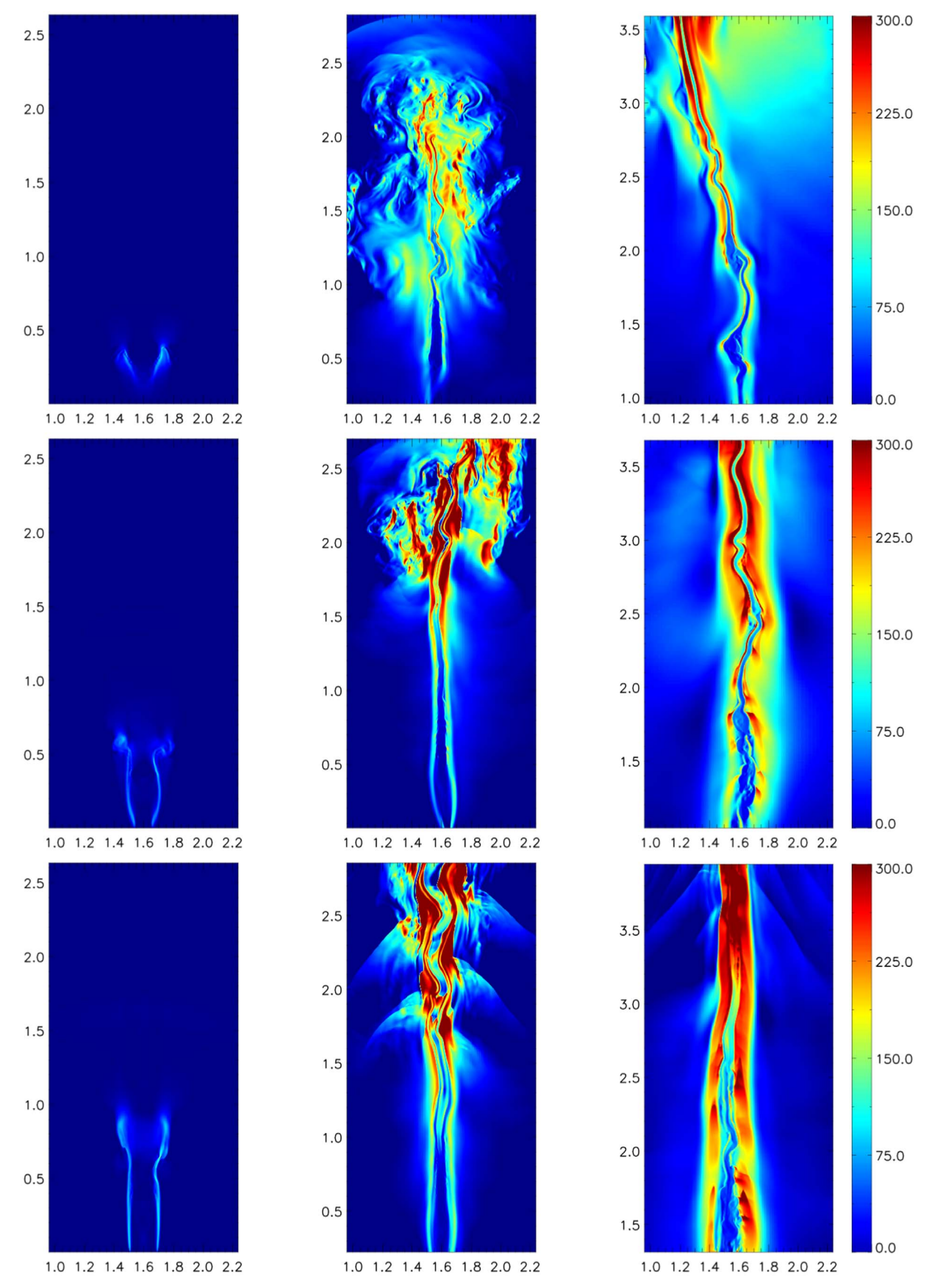


Figure 1. Snapshots of gas density at t = 1 (left), 5 (center), and 10 t_{cc} (right). From top to bottom: CHI300BETA100, CHI300BETA10, and CHI300BETA3. Here and in the figures below, the axes labels denote kpc.



 $\textbf{Figure 2.} \ \, \textbf{Snapshots of Alfv\'en velocity at} \ t = 1 \ (\textbf{left)}, \ 5 \ (\textbf{center}), \ \textbf{and} \ 10 \ t_{\textbf{cc}} \ (\textbf{right)}. \ \textbf{From top to bottom: CHI300BETA100, CHI300BETA10}, \ \textbf{and CHI300BETA3}.$



 $\textbf{Figure 3.} \ \, \textbf{Snapshots of gas} \ \, \textbf{x-velocity at} \ \, t=1 \ \, (\textbf{left}), \ \, \textbf{5} \ \, (\textbf{center}), \ \, \textbf{and} \ \, 10 \ \, t_{cc} \ \, (\textbf{right}). \ \, \textbf{From top to bottom: CHI300BETA100, CHI300BETA10}, \ \, \textbf{and CHI300BETA3}.$

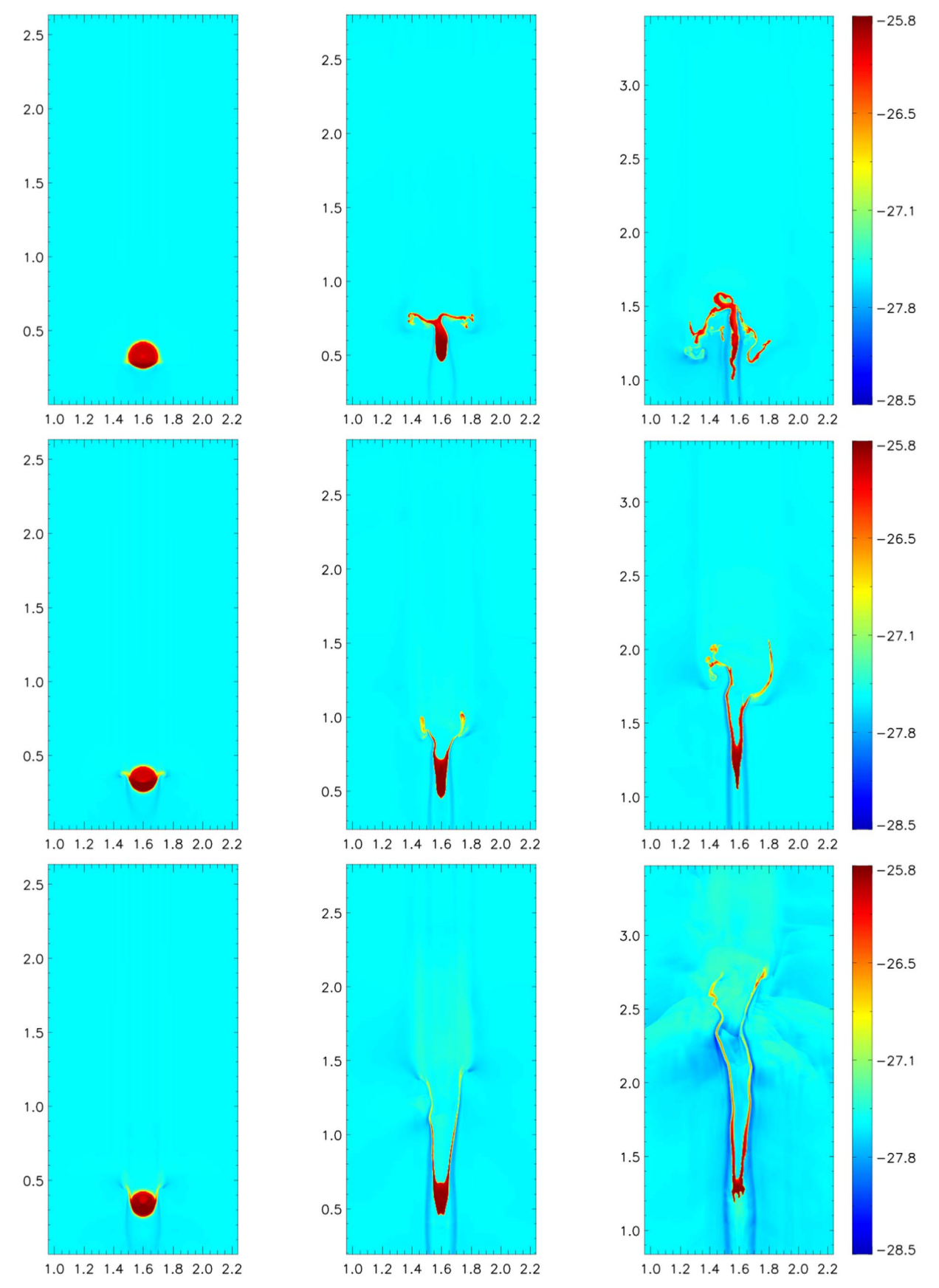
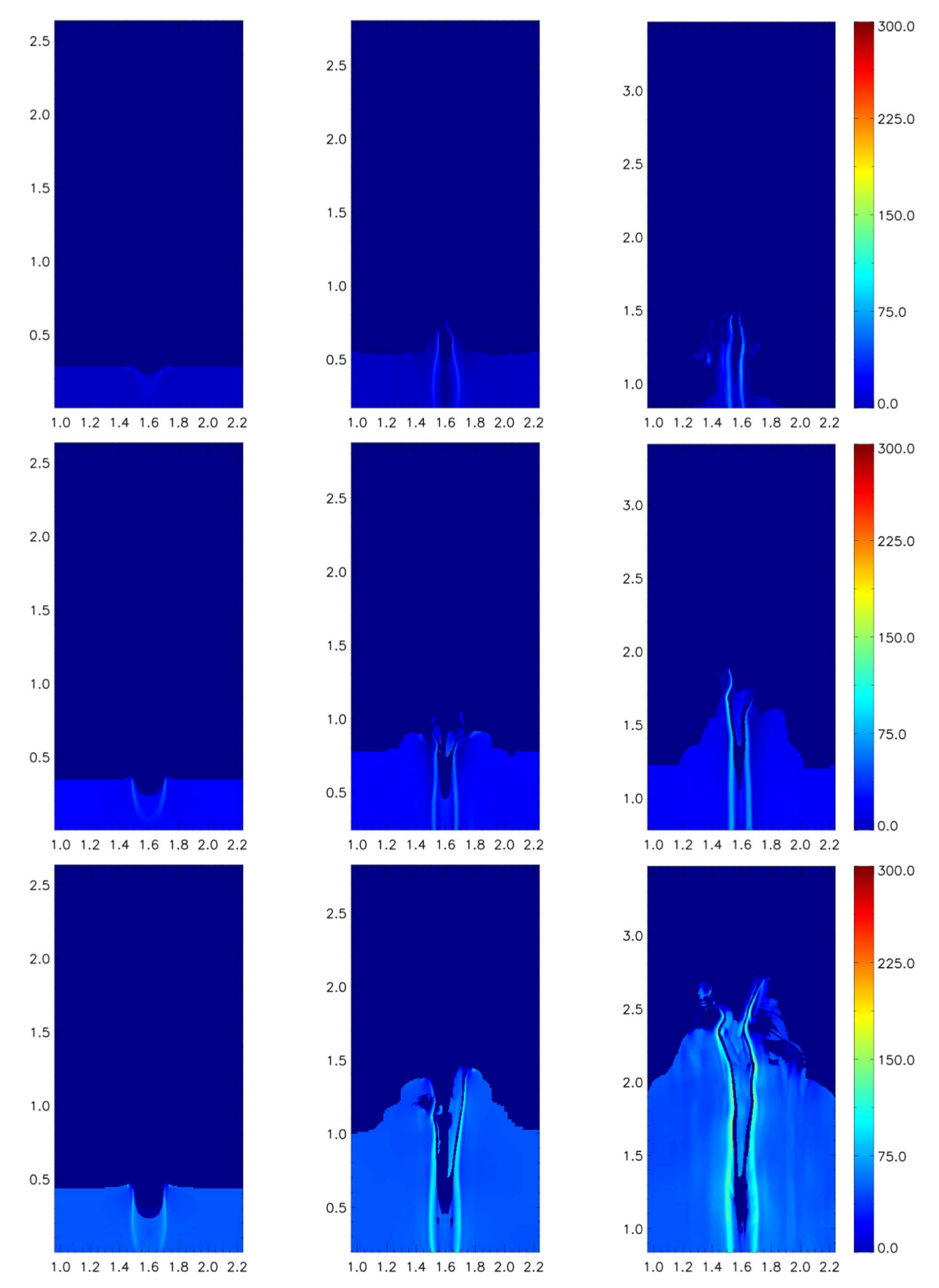


Figure 4. Snapshots of gas density at t = 1 (left), 5 (center), and 10 t_{cc} (right). From top to bottom: CHI30BETA10, CHI30BETA3, and CHI30BETA11.



 $\textbf{Figure 5.} \ \, \textbf{Snapshots of Alfv\'en velocity at} \ \, t=1 \ \, (\textbf{left}), \ \, \textbf{5} \ \, (\textbf{center}), \ \, \textbf{and} \ \, 10 \ \, t_{cc} \ \, (\textbf{right}). \ \, \textbf{From top to bottom: CHI30BETA10, CHI30BETA3, and CHI30BETA1.}$

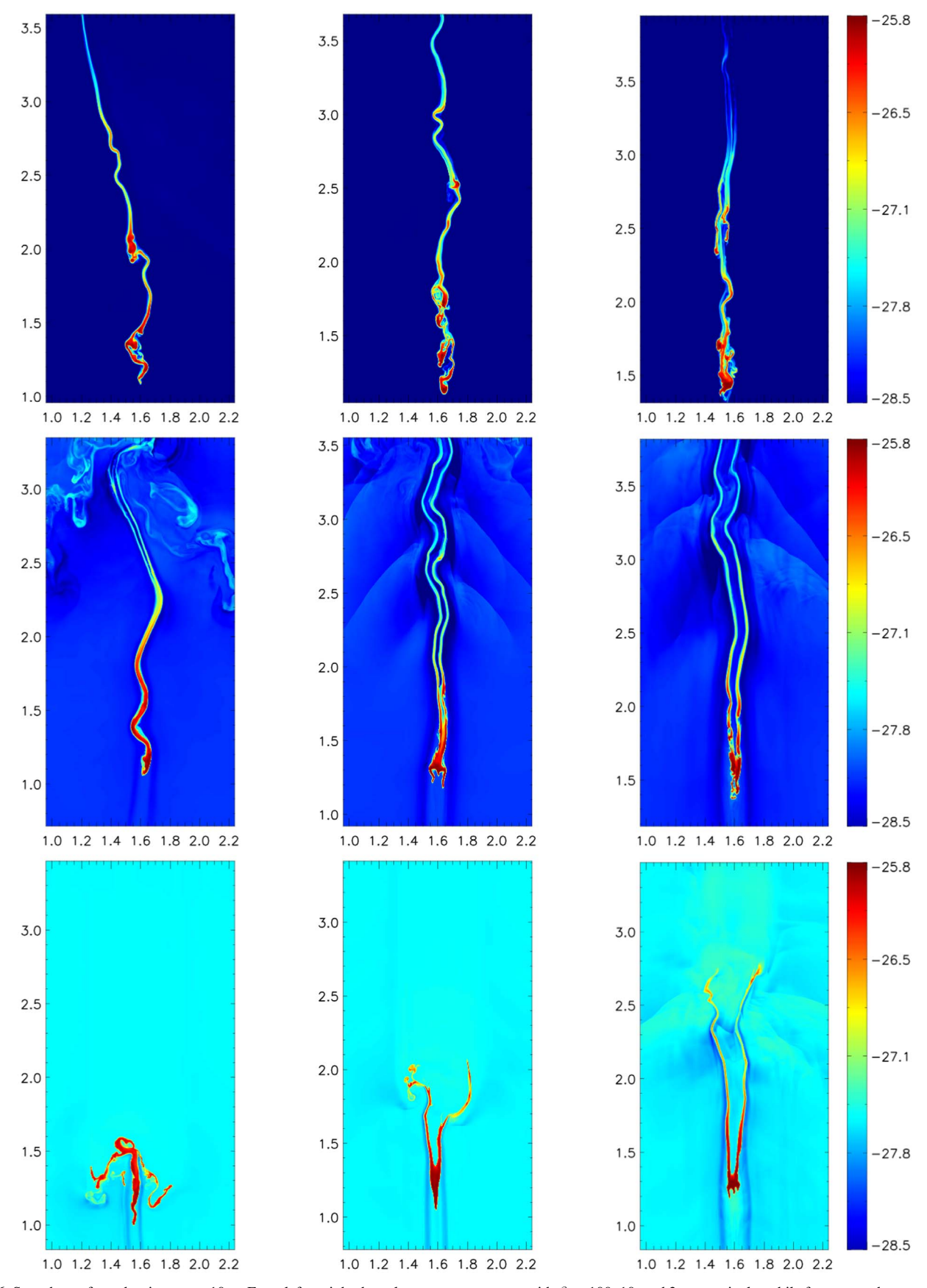


Figure 6. Snapshots of gas density at $t = 10t_{cc}$. From left to right the columns represent runs with $\beta = 100$, 10, and 3, respectively, while from top to bottom, the rows represent runs with $\chi = 300$, 100, and 30.

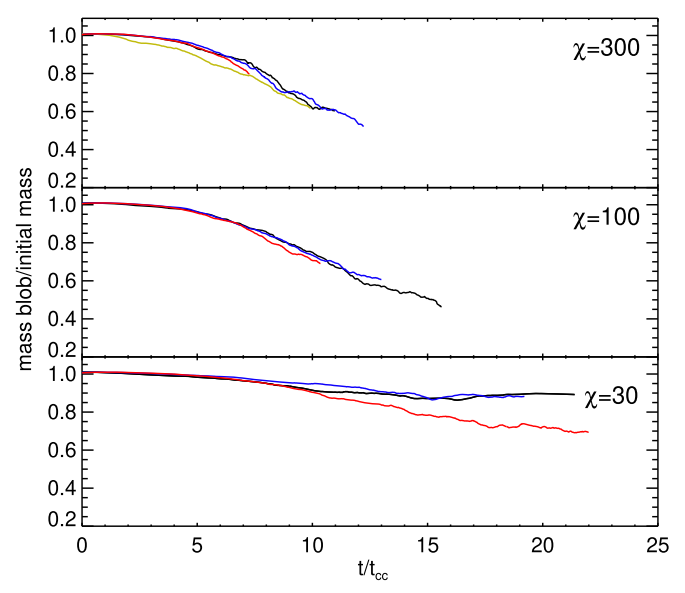


Figure 7. Mass evolution for $\chi=300$ (top), $\chi=100$ (middle), and $\chi=30$ (bottom) as a function of the cloud crushing time. In each panel the different lines correspond to the different values of β : $\beta=100$ (yellow), $\beta=10$ (black), $\beta=3$ (blue), and $\beta=1$ (red).

Alfvén speed. The reason is that at a fixed pressure (CR + thermal), objects with the same size feel the same force, and hence the acceleration is proportional to the inverse of the mass. The higher Alfvén speed leads to a faster propagation of the stripped-off filaments, but since their density remains high, this does not translate into significantly faster mass loss. In every case, the Alfvén speed is sufficient to ensure that the CR pressure at the front of the bubble is roughly the same as at the inner *x*-boundary. This was verified by tracking the pressure at the bow of the cloud.

Comparing between runs with different χ values, we find that when plotted in $t_{\rm cc}$ units, the evolution is similar across models. This means that that cloud disruption timescale goes roughly as $\chi^{1/2}$, as expected in the case of KH-driven mass loss (Chandrasekhar 1961; Brown & Roshko 1974). However, in the low- χ case, the evolution deviates somewhat from this trend, with the clouds surviving longest in the cases with the largest β . These are the cases with the lowest Alfvén speeds, in which the CRs propagate most slowly, and the filaments are the least extended. This delay in the development of an extended shear layer slows the evolution of the KH instability somewhat, preserving the cloud for more cloud crushing times.

3.3. Velocity Evolution

In Figure 8, we show the cloud velocity in terms of the external sound speed as a function of time in units of the cloud crushing time. As a simple model to guide the interpretation of these results, we consider the case in which the cloud cross-section is fixed and the pressure on the cloud is constant and equal to the CR pressure at the boundary. In our two-dimensional configuration, this gives an estimate of

$$v_{0,\text{cl}} = f \frac{2p_{\text{CR}}}{R_{\text{cl}}\rho_{\text{cl}}} t,$$
 (10)

where f is a factor that accounts for the fact that the cloud cross-section drops as it is compressed and stretched during the interaction. Writing t in units of the cloud crushing time and v

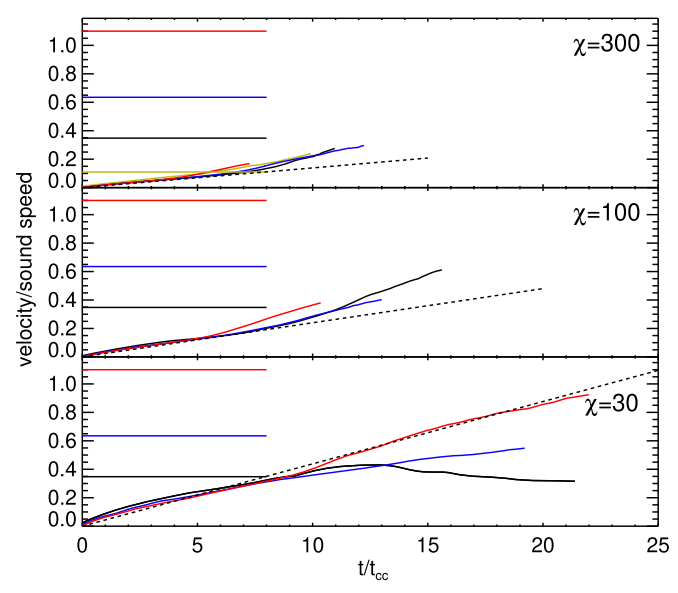


Figure 8. Velocity (in the *x*-direction) for $\chi=300$ (top), $\chi=100$ (middle), and $\chi=30$ (bottom) as a function of the cloud crushing time. In each panel the different lines correspond to the Alfvén speeds corresponding to the different values of β : $\beta=10$ (black), $\beta=3$ (blue), and $\beta=1$ (red). The horizontal lines show the values of the Alfvén speeds in the respective runs, while the dashed line shows the evolution predicted by Equation (11) for f=0.2.

in units of the exterior sound speed, c_s , gives

$$v(t)/c_{\rm s} = f \frac{2p_{\rm CR}\chi^{1/2}}{\rho_{\rm cl}c_{\rm s}^2} \frac{t}{t_{\rm cc}} = f 1.2\chi^{-1/2} \frac{t}{t_{\rm cc}},$$
 (11)

where in the second equality we have taken $c_{\rm s}=15\,{\rm km}$ s $^{-1}\chi^{1/2}$, $p_{\rm CR}=1.4\times10^{-14}$ erg cm $^{-3}$, and $\rho_{\rm cl}=10^{-26}$ g cm $^{-3}$ as in our simulations.

In Figure 8, we overlay this prediction of Equation (11) for f = 0.2 with the results of our simulations. As in Figure 7 we plot the velocity only for the material at or above one-third the original cloud density. Here we see that at early times, this simple model is a good fit to the data, with f = 0.2 accounting for the reduced cross-section of the cloud cause by the lateral squeezing by the CRs. At later times, however, notable deviations arise. In the low- β , high- χ cases, the late-time xvelocities exceed our simple estimate. These are the cases in which the Alfvén speeds are the largest, and a significant fraction of the cloud mass is contained in the filaments, which accelerate faster than the head of the cloud. In the high- β , low- χ cases, on the other hand, the late-time x-velocities are roughly constant. These are the cases in which the clouds start to approach the Alfvén speed, meaning that they are traveling at a rate similar to that of the CRs. This reduces the pressure due to the bottleneck effect, leading to significantly lower xvelocities than estimated in Equation (11).

This general scaling is similar to what is observed in Wiener et al. (2019), in which the velocity of the cloud at a fixed time was found to be proportional to the CR energy density. However, the setup and the driving mechanisms are very different between these simulations. While we hold the energy density of the CRs at the leftmost boundary constant, allowing them to stream onto the grid at the Alfvén speed, Wiener et al. (2019) deposit CRs at a predefined rate in a fixed portion of the grid. In addition, the acceleration of the cloud is both due the bottleneck effect studied here, as well as acceleration of the low density medium, which does not arise in our work due to the

numerical choices described above. Finally, unlike Wiener et al. (2019), we do not switch off the CR pressure after a finite time, and thus we achieve velocities of the order of the Alfvén velocities even for smaller CR fluxes than those they investigated. Nevertheless, in both cases the velocity of the cloud at a fixed time is proportional to $p_{\rm CR}$ as arises in pressure estimate as in Equation (10), rather than proportional to $p_{\rm CR}^{1/2}$ as would occur in a situation in which a fixed fraction of the CR energy density is being transferred to the cloud.

3.4. The Effect of Radiative Cooling

In order to assess the effect of cooling, we ran a selection of runs with radiative cooling switched off. Radiative cooling is known to delay mixing by keeping the boundary layer thinner and by preventing the growth of the KH instability (e.g., Vietri et al. 1997). However, once the KH instability turns nonlinear, it is not clear how effectively cooling can suppress mixing (Micono et al. 2000).

In Figure 9 we show the gas density at $=10t_{\rm cc}$, from nine such simulations. Unlike ram-pressure acceleration, acceleration by the CRs does not produce shocks that heat the cloud, and must be radiated away to avoid disruption. In fact, we find that switching off radiative cooling does not lead to qualitatively different behavior. In this case, the filaments that are smoother than in the previous runs, suggesting that cooling causes more fragmentation at the shear interface between the cloud and the ambient medium. However, the overall morphology of the clouds are similar, which also translates into a similar evolution of the mass and the velocity of the cloud. This is in agreement with Wiener et al. (2019, see their Figure 14 that, however, still includes CR heating).

In Figure 10, we show the fraction of the mass retained by the cloud in each of these runs as a function of time in units of the cloud crushing time, $t_{\rm cc}$. Again, this figure is very similar to Figure 7. There are some differences, most notably for $\chi=30$, where the mass declines more quickly than in the case with radiative cooling. Also, for $\chi=300$ and $\beta=100$ the mass of the cloud declines more quickly than in the case with radiative cooling. In this run, which is closest to the pure hydrodynamics case, radiative cooling is most needed to keep the cloud intact and impede the ablation of gas. For the cases with lower β this is less pronounced because the magnetic field acts to keep the cloud from disrupting.

Wiener et al. (2019) stress that the inclusion of radiative cooling prevents the disruption of the cloud by CR heating. Such heating leads to an additional term, $\mathcal{H}_{CR} = -v_A \cdot \nabla p_{CR}$ (Wentzel 1971), that goes into Equation (8) but is not included in the work presented here. However, the disruption timescale via CR heating for our choice of parameters is of the order of 100 Myr, which is too long to have an effect on cloud evolution on the timescales relevant for our simulations.

Finally, to assess the impact of the numerical switch that allows acceleration by CRs only on cells whose density lies at least 10% above the ambient density, we carried out a comparison run for the $\chi=100$, $\beta=10$ case in which the switch was turned off, but the regularization was maintained. In this run, the mass-loss rate and acceleration of the blob are very similar to the fiducial case at early times ($t \leq 5t_{\rm cc}$), and slightly greater (by about a factor of 1.5) at later times. These differences are small enough such that they do not affect any of the conclusions described above. Furthermore, as they are caused by CRs scattering off of numerical noise, they are likely

to be resolution dependent, and smaller in higher-resolution simulations.

4. Conclusions

The acceleration of cold clouds by CRs is an important topic in understanding the multiphase evolution of starburst-driven galactic winds. Such outflows contain not only hot $\approx 10^7 - 10^8$ K material, with sounds speeds that are comparable to the outflow velocities, but also $\approx 10^4$ K clouds, whose sounds speeds are less than an order of magnitude smaller. While this supersonic gas is often assumed to be accelerated by the hot wind, such interactions tend to shred and evaporate the clouds before significant acceleration is achieved. At the same time, the supernovae that drive starbursts also generate a large number of CRs, which can potentially accelerate cold gas while avoiding the destructive processes observed in ram-pressure acceleration.

To better understand this possibility, we have simulated the interactions of cold clouds with CR gradients of the type expected in galactic winds. Using the FLASH AMR MHD code, we exposed cold clouds to CR gradients that stream with Alfvén speeds along the magnetic field lines. These 2D simulations include radiative cooling, but do not include explicit CR heating, and they include an important switch that suppresses the acceleration of the ambient medium by the streaming against sound waves and weak shocks.

In this case, the CRs stream toward the cloud at the Alfvén speed, which decreases dramatically at the cloud boundary, leading to a bottleneck in which the CRs pile up in front of the cloud, building up pressure. At the same time, the CRs start to stream along the sides of the cloud, causing the cloud to be compressed in the perpendicular direction. The low densities and high field values in this boundary layer cause the Alfvén speed to go up dramatically, leading to significant shear. By sampling a large range of the density contrasts, χ , and ratios of thermal to magnetic pressure, β , we are able to study how these effects lead to acceleration and mass loss over the conditions experienced by cold clouds.

The major results from these simulations are:

- 1. Cloud destruction occurs primarily due to shear in the filaments that arise in the boundary layer. As expected from the KH instability, this leads to a mass-loss rate in units of $t_{\rm cc}$ that is largely independent of both χ and β . In most cases, the clouds lose half their mass by $\approx 12t_{\rm cc}$, although the mass-loss rate is slower in the cases with very low χ and β . These are the cases with the lowest Alfvén speeds, in which the CRs take the most time to propagate, the filaments are the least extended, and the KH shear layer develops most slowly.
- 2. The acceleration of the cloud is consistent with a simple model in which CR pressure is constant and the cloud cross-section is ≈ 0.2 of its initial cloud size. This reduction in the size of the cloud perpendicular to the flow is caused by the pressure of the CRs streaming around the cloud, and it leads to a cloud velocity of $\approx 0.25c_s\chi^{-1/2}t/t_{cc}$. In most cases, this is long enough to allow for cloud acceleration to a significant fraction of the exterior sound speed. However, in cases in which clouds approach the Alfvén speed, they begin to outrun the impinging CRs, leading to more gradual acceleration.

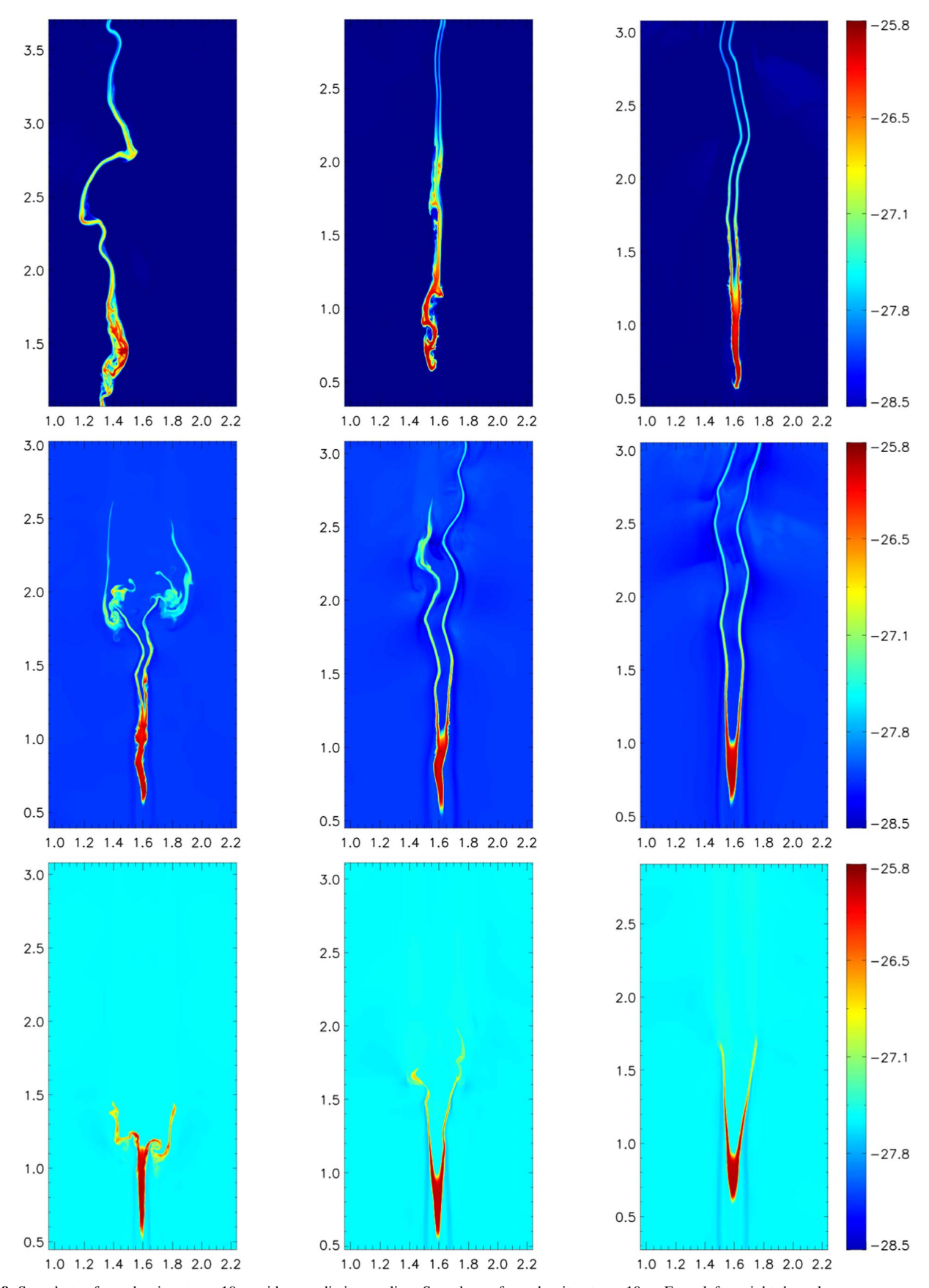


Figure 9. Snapshots of gas density at $t = 10t_{cc}$ with no radiative cooling. Snapshots of gas density at $t = 10t_{cc}$. From left to right the columns represent runs with $\beta = 100$, 10, and 3, respectively, while from top to bottom, the rows represent runs with $\chi = 300$, 100, and 30. The axes labels denote kpc.

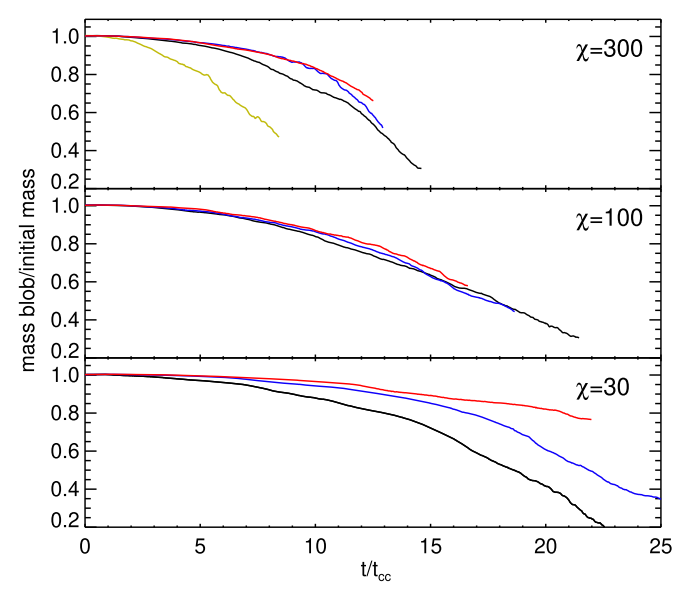


Figure 10. Mass evolution for $\chi=300$ (top), $\chi=100$ (middle), and $\chi=30$ (bottom) as a function of the cloud crushing time in the absence of radiative cooling. In each panel the different lines correspond to the different values of β : $\beta=100$ (yellow), $\beta=10$ (black), $\beta=3$ (blue), and $\beta=1$ (red).

- 3. Radiative cooling has relatively little impact on cloud evolution. By carrying out comparison runs in which it was switched off, we found that the overall cloud morphology is somewhat smoother than in runs with cooling. However, mass-loss rates and accelerations were similar in both cases.
- 4. Together, these results show that CRs, if acting as the primary sources of momentum input, are capable of accelerating clouds to velocities comparable to those observed in galaxy outflows.

There are, however, a number of important caveats to this conclusion. Our treatment of CR transport does not consider the effects of wave damping, which may become relevant inside the cold cloud if Alfvén waves suffer significant ionneutral damping. This could increase the CR energy density inside the cloud at the beginning of the interaction. Our results also do not include CR heating, which can have a significant impact for more extreme CR pressure gradients and on longer timescales than the ones simulated here. Our simulations assume that magnetic fields penetrate the clouds, which is a necessary condition to produce CR bottlenecks. Finally, our simulations are two-dimensional, due to restrictive time step requirements, which may alleviated in the future by a new method to compute CR streaming that is based on a radiative transfer method (Jiang & Oh 2018; Thomas & Pfrommer 2019).

A key difference between our work and the work described in Wiener et al. (2019) is due to our choice of regularization criteria and the threshold on the CR gradient in the *x*-direction. Together, these prevent the ambient medium from being significantly accelerated by CRs, in contrast to the significant acceleration of the ambient medium seen in this previous work. The acceleration of the exterior medium causes substantial shear at the cloud-environment interface, influencing the cloud evolution in ways that are distinct and difficult to disentangle from effects due to the CR pressure.

While the CR acceleration of the exterior medium remains an open question, in will be subdominant with respect to the acceleration of the ambient medium due its thermal pressure. This is because, unlike cold clouds, the hot medium has a sound speed much higher than the escape velocity of the host galaxy, and it can expand freely into the surrounding environment. This means that cold cloud evolution in galactic outflows will likely depend on the combination of CRs and gas shear that is dependent on the particulars of the starburst itself and the magnetic field structure near the clouds, and that cloud survival will depend on the evolution of the KH instability in this complex situation. A better understanding of such interactions will continue to improve our understanding of the cold clouds observed in starburst-driven galactic winds.

We thank the reviewer for a very constructive review. Part of this work was performed at the Turbulent Life of Cosmic Baryons program at the Aspen Center for Physics, which is supported by National Science Foundation grant PHY-1607611. We thank Josh Wiener and Ellen Zweibel for helpful discussions. The authors gratefully acknowledge the Gauss Centre for Supercomputing e.V. (www.gauss-center.eu) for funding this project (16072) by providing computing time through the John von Neumann Institute for Computing (NIC) on the GCS Supercomputer JUWELS at Jülich Supercomputing Centre (JSC). The FLASH code was developed in part by the DOE-supported Alliances Center for Astrophysical Thermonuclear Flashes (ASC) at the University of Chicago. E.S. was supported by NSF grant AST-1715876.

ORCID iDs

Marcus Brüggen https://orcid.org/0000-0002-3369-7735 Evan Scannapieco https://orcid.org/0000-0002-3193-1196

References

```
Bolatto, A. D., Warren, S. R., Leroy, A. K., et al. 2013, Natur, 499, 450
Booth, C. M., Agertz, O., Kravtsov, A. V., & Gnedin, N. Y. 2013, ApJL,
Bregman, J. N. 2004, in High Velocity Clouds, ed. H. van Woerden et al.
  (Dordrecht: Kluwer Academic), 341
Breitschwerdt, D., McKenzie, J. F., & Voelk, H. J. 1993, A&A, 269, 54
Brown, G. L., & Roshko, A. 1974, JFM, 64, 775
Brüggen, M., & Scannapieco, E. 2016, ApJ, 822, 31
Chandrasekhar, S. 1961, Hydrodynamic and Hydromagnetic Stability (Oxford:
  Clarendon)
Chevalier, R. A., & Clegg, A. W. 1985, Natur, 317, 44
Cottle, J., Scannapieco, E., Brüggen, M., Banda-Barragán, W., & Federrath, C.
  2020, ApJ, 892, 59
Davé, R., Oppenheimer, B. D., & Finlator, K. 2011, MNRAS, 415, 11
Dorfi, E. A., & Breitschwerdt, D. 2012, A&A, 540, A77
Everett, J. E., Zweibel, E. G., Benjamin, R. A., et al. 2008, ApJ, 674, 258
Farber, R., Ruszkowski, M., Yang, H. Y. K., & Zweibel, E. G. 2018, ApJ,
Ferland, G. J., Korista, K. T., Verner, D. A., et al. 1998, PASP, 110, 761
Fryxell, B., Olson, K., Ricker, P., et al. 2000, ApJS, 131, 273
Girichidis, P., Naab, T., Hanasz, M., & Walch, S. 2018, MNRAS, 479, 3042
Gray, W. J., & Scannapieco, E. 2010, ApJ, 718, 417
Gronke, M., & Oh, S. P. 2018, MNRAS, 480, L111
Gronke, M., & Oh, S. P. 2020, MNRAS, 492, 1970
Hanasz, M., Lesch, H., Naab, T., et al. 2013, ApJL, 777, L38
Heckman, T. M. 2002, in ASP Conf. Ser. 254, Extragalactic Gas at Low
  Redshift, ed. J. S. Mulchaey & J. T. Stocke (San Francisco, CA: ASP), 292
Heesen, V., Whitler, L., Schmidt, P., et al. 2019, A&A, 628, L3
Holguin, F., Ruszkowski, M., Lazarian, A., Farber, R., & Yang, H. Y. K. 2019,
       RAS, 490, 1271
Hopkins, P. F., Quataert, E., & Murray, N. 2011, MNRAS, 417, 950
Huang, S., Katz, N., Scannapieco, E., et al. 2020, MNRAS, 497, 2586
```

Irwin, J. A., English, J., & Sorathia, B. 1999, AJ, 117, 2102

Jana, R., Gupta, S., & Nath, B. B. 2020, MNRAS, 497, 2623

```
Jiang, Y.-F., & Oh, S. P. 2018, ApJ, 854, 5
Klein, R. I., McKee, C. F., & Colella, P. 1994, ApJ, 420, 213
Lacki, B. C., Thompson, T. A., & Quataert, E. 2010, ApJ, 717, 1
Martin, C. L. 1999, ApJ, 513, 156
Martin, C. L., Shapley, A. E., Coil, A. L., et al. 2012, ApJ, 760, 127
McKenzie, J. F., & Webb, G. M. 1984, JPlPh, 31, 275
Micono, M., Bodo, G., Massaglia, S., et al. 2000, A&A, 360, 795
Murray, N., Ménard, B., & Thompson, T. A. 2011, ApJ, 735, 66
Pettini, M., Shapley, A. E., Steidel, C. C., et al. 2001, ApJ, 554, 981
Rupke, D. S., Veilleux, S., & Sanders, D. B. 2005, ApJS, 160, 115
Ruszkowski, M., Yang, H. Y. K., & Zweibel, E. 2017, ApJ, 834, 208
Salem, M., & Bryan, G. L. 2014, MNRAS, 437, 3312
Samui, S., Subramanian, K., & Srianand, R. 2018, MNRAS, 476, 1680
Scannapieco, E. 2013, ApJL, 763, L31
Scannapieco, E. 2017, ApJ, 837, 28
Scannapieco, E., & Brüggen, M. 2015, ApJ, 805, 158
Schneider, E. E., Robertson, B. E., & Thompson, T. A. 2018, ApJ, 862, 56
Sharma, P., Colella, P., & Martin, D. F. 2009, SIAM J. Sci. Comput., 32, 3564
Silich, S., Tenorio-Tagle, G., & Muñoz-Tuñón, C. 2003, ApJ, 590, 791
Skilling, J. 1975, MNRAS, 172, 557
```

```
Soto, K. T., & Martin, C. L. 2012, ApJS, 203, 3
Strickland, D. K., & Heckman, T. M. 2009, ApJ, 697, 2030
Thomas, T., & Pfrommer, C. 2019, MNRAS, 485, 2977
Thompson, T. A., Quataert, E., & Murray, N. 2005, ApJ, 630, 167
Thompson, T. A., Quataert, E., Zhang, D., & Weinberg, D. H. 2016, MNRAS,
Tremonti, C. A., Moustakas, J., & Diamond-Stanic, A. a. M. 2007, ApJL,
  663, L77
Tumlinson, J., Peeples, M. S., & Werk, J. K. 2017, ARA&A, 55, 389
Veilleux, S., Cecil, G., & Bland-Hawthorn, J. 2005, ARA&A, 43, 769
Veilleux, S., Maiolino, R., Bolatto, A. D., & Aalto, S. 2020, A&ARv, 28, 2
Vietri, M., Ferrara, A., & Miniati, F. 1997, ApJ, 483, 262
Walter, F., Weiss, A., & Scoville, N. 2002, ApJL, 580, L21
Wang, B. 1995, ApJL, 444, L17
Wang, X., & Fields, B. D. 2018, MNRAS, 474, 4073
Wentzel, D. G. 1971, ApJ, 163, 503
Wiegert, T., Irwin, J., Miskolczi, A., et al. 2015, AJ, 150, 81
Wiener, J., Oh, S. P., & Zweibel, E. G. 2017, MNRAS, 467, 646
Wiener, J., Zweibel, E. G., & Ruszkowski, M. 2019, MNRAS, 489, 205
Wiersma, R. P. C., Schaye, J., & Smith, B. D. 2009, MNRAS, 393, 99
```